JOURNAL OF THERMOPHYSICS AND HEAT TRANSFER
Vol. 17, No. 2, April–June 2003

Calculation of Shock Shapes over Sharp Cone in Intermediate Hypersonic Airflow

Michiko Furudate,[*] Satoshi Nonaka,[†] and Keisuke Sawada[‡]
Tohoku University, Sendai 980-8579, Japan

Shock shapes over a sharp cone in the intermediate hypersonic flow regime are calculated to examine the validity of the existing two-temperature thermochemical model. Two different apex angles are considered in the calculations: one with a half-angle of 30 deg and the other with 45 deg. The calculations for these geometries are carried out for several different static pressure values at the flight velocity of about 3.0 km/s. The calculated shock layer thickness is compared with the corresponding experimental data obtained in a ballistic range. The results show that the two-temperature model well reproduces the experimental data for the flow conditions in which chemical reactions as well as vibrational excitations are absent. However, the calculated shock layer thickness tends to be thinner than the experimental data for the flow conditions in which vibrational excitation begins to occur. It is implied that vibrational relaxation has a close connection with the thinner shock layer. The study confirms our previous results that the shock layer thickness over a sphere in the same velocity range can be underestimated in the calculation using the existing two-temperature model.

Nomenclature

A_i = coefficients in Eq. (6) and Table 2
C_f = coefficients in Eq. (2) and Table 1
E_v = vibrational–electronic excitation energy per unit volume, J/m^3
E_v^* = vibrational–electronic excitation energy per unit volume at local translational–rotational temperature T, J/m^3
K_{eq} = equilibrium constant, mole/m^3
k_b = backward reaction rate, m^3/mole · s
k_f = forward reaction rate, m^3/mole · s or m^6/mole^2 · s
M = collision partners in dissociation/recombination reactions
M_s = atomic/molecular weight of species s, kg/mole
p = pressure, Pa
$\hat{R}$ = universal gas constant, 8.314 J/mole · K
r = radius of blunted tip of cone, mm
T = translational–rotational temperature, K
T_v = vibrational–electronic excitation temperature, K
T_w = wall temperature, K
U = velocity, m/s
$W_{\mathrm{C-v}}$ = chemical reaction–vibrational energy transfer rate, J/m^3 · s
W_s = mass source term of species s per unit volume, kg/m^3 · s
W_v = vibrational–electronic excitation energy source term, J/m^3 · s
$W_{\mathrm{v-T}}$ = vibrational–translational energy transfer rate, J/m^3 · s
x = distance along cone axis measured from tip of cone, mm
α = pitch angle, deg
β = yaw angle, deg
δ = shock layer thickness, mm
θ_D = characteristic reaction temperature
η = coefficients in Eq. (2) and Table 1
ρ = density, kg/m^3
τ_c = collision time, s
τ_{MW} = vibrational relaxation time according to Millikan–White correlation,[20] s
ω = constant in Eq. (11)

Subscripts

s = species
shock = shock location
∞ = freestream

Introduction

LAUNCH vehicles with airbreathing engines have been considered as promising candidates for reusable launch systems in the next generation. Such a vehicle is planned to function in the speed range between 2.5 and 4.5 km/s. High-temperature phenomena, such as chemical reactions, thermal excitations, and their nonequilibrium effects, are less significant in this speed range. However, sophisticated vehicle design needs to account for them. For example, the performance of an airbreathing engine can be seriously affected by possible boundary-layer separation in the inlet. The separation point can be moved due to the high-temperature phenomena. Chemical reactions and thermal excitations tend to absorb a significant amount of heat and, thus, to reduce the temperature and stabilize the boundary layer. The high-temperature phenomena can also affect the pressure distribution on the body surface, resulting in altering the aerodynamic characteristics of the vehicle. Therefore, a reliable computational fluid dynamics (CFD) code for computing flows involving high-temperature phenomena in the so-called intermediate hypersonic regime is required.

Thermochemical models used in the hypersonic CFD codes must be validated carefully using reliable experimental data. Recently, measurements of the shock standoff distances for a sphere and the shock shapes for a sharp cone in the intermediate hypersonic flow have been conducted using a ballistic range at the Shock Wave

---

Presented as Paper 99-3686 at the AIAA 33rd Thermophysics Conference, Norfolk, VA, 28 June–1 July 1999; received 5 December 2001; revision received 4 November 2002; accepted for publication 5 November 2002. Copyright © 2002 by the American Institute of Aeronautics and Astronautics, Inc. All rights reserved. Copies of this paper may be made for personal or internal use, on condition that the copier pay the $10.00 per-copy fee to the Copyright Clearance Center, Inc., 222 Rosewood Drive, Danvers, MA 01923; include the code 0887-8722/03 $10.00 in correspondence with the CCC.

[*] Graduate Student, Department of Aeronautics and Space Engineering; currently, Research Fellow of the Japan Society for Promotion of Science, The Institute of Space and Astronautical Sciences, 3-1-1, Yoshinodai, Sagamihara 229-8510, Japan. Member AIAA.

[†] Graduate Student, Department of Aeronautics and Space Engineering; currently, Research Associate, Research Division for Space Systems Engineering, The Institute of Space and Astronautical Science, 3-1-1, Yoshinodai, Sagamihara 229-8510, Japan. Member AIAA.

[‡] Professor, Department of Aeronautics and Space Engineering. Associate Fellow AIAA.

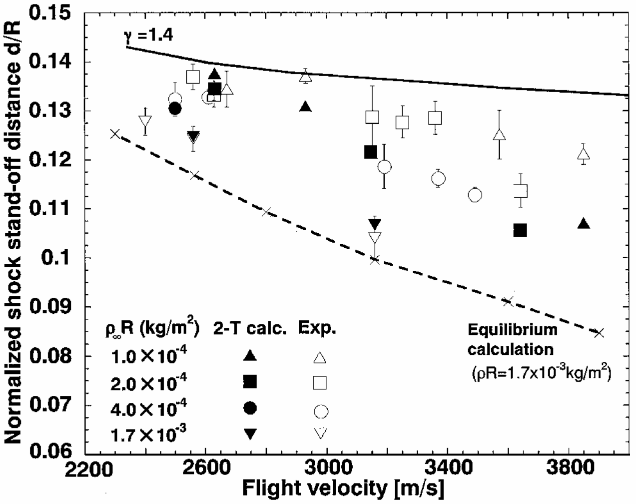

Fig. 1 Summary of comparisons of shock standoff distances for sphere in intermediate hypersonic regime.[5]

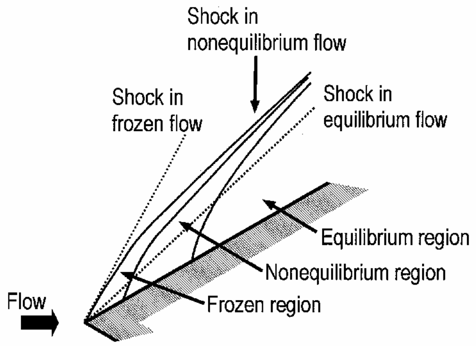

Fig. 2 Schematic of the flowfield over a sharp cone.

Research Center (SWRC), Institute of Fluid Science, Tohoku University, Japan.[1,2] In the ballistic range, the freestream condition can be completely characterized because a projectile flies in a quiescent gas in the test section. Thus, the ballistic range can provide reliable experimental data for validating hypersonic CFD codes.

Validation of the nonequilibrium thermochemical models for the hypersonic CFD codes can be conveniently accomplished by choosing the shock standoff distance for the sphere as a reference value.[3] The shock standoff distance is determined by the density profile, which critically depends on how chemical reactions and thermal excitations of the gas proceed in the shock layer. In our previous work, efforts were made to examine the existing two-temperature model[4] by using ballistic range data of the shock standoff distances over spheres in intermediate hypersonic flows. It was found that the two-temperature model was likely to underestimate the shock standoff distance for the conditions with the flight velocity exceeding 3.0 km/s, as summarized in Fig. 1 (Ref. 5.)

The shock shape over a sharp cone also serves as another reference value to validate thermochemical models.[3] The shock wave developed over a sharp cone can be curved when chemical reactions and vibrational excitations in the shock layer take place in finite rates, as shown in Fig. 2. The shock angle decreases from that of the frozen flow to that of the equilibrium flow with increasing axial distance from the tip of the cone.[6] Therefore, the validity of the nonequilibrium thermochemical models can be examined by comparing the shock shape obtained in calculation with experimental data.

In the present study, we attempt to calculate thermochemical nonequilibrium flowfields over sharp cones. By comparing with the shock shapes obtained in the ballistic range experiment conducted at SWRC,[2] we critically examine the behavior of the existing two-temperature model in the intermediate hypersonic regime. Because of the conical shape of the shock wave, the temperature in the shock layer is lower than that in the shock layer over a sphere, which was studied in our previous study. This allows us to examine the flowfield that is vibrationally excited but chemically frozen. The effect of bluntness of the tip, as well as wall temperature on the shock shape, is also examined.

Table 1 Forward reaction rate coefficients (Ref. 7)

Reaction	M	C_f	η	θ_D
$O_2 + M \rightleftharpoons O + O + M$	O_2	2.0×10^{15}	−1.5	59,500
	N_2	2.0×10^{15}	−1.5	59,500
	NO	2.0×10^{15}	−1.5	59,500
	O	1.0×10^{16}	−1.5	59,500
	N	1.0×10^{16}	−1.5	59,500
$N_2 + M \rightleftharpoons N + N + M$	O_2	7.0×10^{15}	−1.6	113,200
	N_2	7.0×10^{15}	−1.6	113,200
	NO	7.0×10^{15}	−1.6	113,200
	O	3.0×10^{16}	−1.6	113,200
	N	3.0×10^{16}	−1.6	113,200
$NO + M \rightleftharpoons N + O + M$	O_2	5.0×10^{9}	0.0	75,500
	N_2	5.0×10^{9}	0.0	75,500
	NO	1.1×10^{11}	0.0	75,500
	O	1.1×10^{11}	0.0	75,500
	N	1.1×10^{11}	0.0	75,500
$N_2 + O \rightleftharpoons NO + N$	——	6.4×10^{11}	−1.0	38,400
$NO + O \rightleftharpoons O_2 + N$	——	8.4×10^{6}	0.0	19,450

Numerical Method

Five neutral air species, that is, N_2, O_2, N, O, and NO, are considered in the calculation. The governing equations are the three-dimensional Navier–Stokes equations. The set of equations consists of global mass, species mass, momentum, total energy, and vibrational–electronic energy conservation equations. When the concept of the elementary ratio conservation law is used, only three species mass conservation equations corresponding to O, N, and NO are solved.[7]

The following five chemical reactions are considered:

$$\begin{gathered} O_2 + M \leftrightarrow O + O + M \\ N_2 + M \leftrightarrow N + N + M \\ NO + M \leftrightarrow N + O + M \\ N_2 + O \leftrightarrow NO + N \\ NO + O \leftrightarrow O_2 + N \end{gathered} \tag{1}$$

The forward reaction rates are written in the form

$$k_f(T_a) = C_f T_a^{\eta} \exp(-\theta_D / T_a) \tag{2}$$

We employ the reaction rate coefficients proposed for the two-temperature model by Park,[7] as given in Table 1. For dissociation reactions, the rate controlling temperature is defined by

$$T_a = \sqrt{T T_v} \tag{3}$$

and for exchange and recombination reactions,

$$T_a = T \tag{4}$$

The backward reaction rates are written in the form

$$k_b(T) = k_f(T) / K_{\text{eq}}(T) \tag{5}$$

where

$$K_{\text{eq}} = \exp\left[A_1 Z + A_2 + A_3 \ln(1/Z) + A_4/Z + A_5 / Z^2\right] \tag{6}$$

and

$$Z = 10{,}000/T \tag{7}$$

The coefficients for the equilibrium constants in Eq. (6) are given in Table 2.

Table 2 Constants for equilibrium constants (Ref. 7)

Reaction	A_1	A_2	A_3	A_4	A_5
1	0.553880	16.275511	1.776300	−6.57200	0.031445
2	1.53510	15.4216	1.2993	−11.494	−0.00698
3	0.558890	14.53108	0.553960	−7.53040	−0.014089
4	0.976460	0.890430	0.745720	−3.96420	0.007123
5	0.004815	−1.74430	−1.22270	−0.95824	−0.045545

The vibrational source term can be written as a sum of two terms as

$$W_v = W_{\mathrm{v-T}} + W_{\mathrm{C-v}} \tag{8}$$

The first term in the right-hand side denotes the energy transfer between translational and vibrational energy modes and is given by

$$W_{\mathrm{v-T}} = \sum_s W_{\mathrm{v-T}s} = \sum_s \frac{E^*_{vs}(T) - E_{vs}}{\tau_{\mathrm{MW}s} + \tau_c} \left| \frac{T_{\mathrm{shock}} - T_v}{T_{\mathrm{shock}} - T_{v\,\mathrm{shock}}} \right|^{S-1} \tag{9}$$

where

$$S = 3.5\exp(-5000/T_{\mathrm{shock}}) \tag{10}$$

The vibrational energy source due to chemical reactions is described in the form

$$W_{\mathrm{C-v}} = \sum_s W_{\mathrm{C-v}s} = \sum_s \omega\theta_{Ds}\frac{\hat{R}}{M_s}W_s \tag{11}$$

The removed or gained vibrational energy through dissociation or recombination reactions are set to be 30% of the corresponding dissociation energy, that is, $\omega = 0.3$ in Eq. (11), as suggested by Sharma.[8]

The molecular viscosity for air species is given by the Blottner et al. model[9] and the thermal conductivity by Eucken's relation (see Ref. 10). Those transport properties for air are obtained from Wilke's empirical mixing formula.[11] We assume the diffusion coefficients to be constant for all species with a constant Schmitt number of 0.5.

The numerical scheme is based on the cell-vertex finite volume method. We employ a prismatic unstructured mesh system for avoiding grid singular lines often appearing in structured mesh systems, while retaining spatial accuracy in a thin boundary layer. The convective numerical flux is calculated by AUSM-DV upwind scheme.[12] The dependent variables along mesh lines normal to the body surface are interpolated by the conventional MUSCL approach,[13] and Barth's method[14] is used in each unstructured mesh layer. The two-level, second-order, explicit Runge–Kutta method is used for time integration. The diagonal point implicit method[15] is employed for improving stability in the integration of source terms. For the convergence acceleration, the local time-stepping method is used.

Test Conditions

The calculations are carried out for conditions that correspond to the ballistic range experiments conducted at SWRC. The projectiles used in the experiments are cone–cylinders with the half-apex angles of 30 and 45 deg. The base diameter of the cones is 30 mm. In the calculations, only the conical part of the projectile is considered. Figure 3 shows an example of prismatic unstructured computational mesh system used in the calculation. The number of the prismatic cells is 6196 × 50 for the 30 deg and 4612 × 50 for the 45-deg sharp cones. The computational cells in the direction departing from the cone are clustered to the shock position as well as in the boundary layer to attain higher spatial resolution.

Table 3 Test conditions for sharp cone

	Case			
Parameter	1-1	1-2	2-1	2-2
Half angle, deg	30	30	45	45
ρ_∞, kg/m^3	0.0714	0.119	0.0238	0.0714
p_∞, Pa	6000	10,000	2000	6000
U_∞, km/s	2.82	2.75	3.31	3.15
α, deg	–0.3	−1.6	−1.4	−1.4
β, deg	5.7	3.5	0.0	1.9

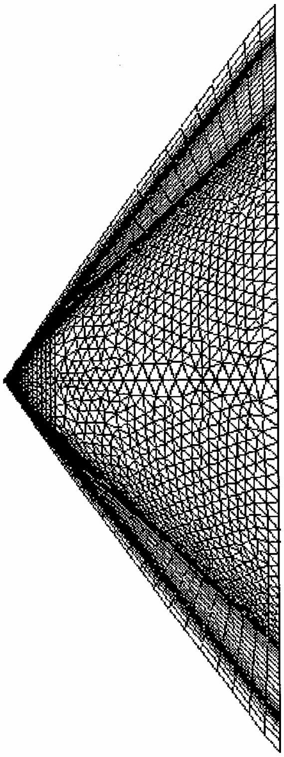

Fig. 3 Example of prismatic mesh used in the calculation (2361 × 51 points).

Calculations are carried out for four different conditions summarized in Table 3, which are chosen from the experimental data. The flight velocities are in the same range in each set of conditions. The test section is filled with a dry air consisting of 23.3% of O_2 and 76.7% of N_2 by mass. It is assumed that the translational and the vibrational temperatures in the freestream are in equilibrium at 293 K and that the projectile has an isothermal wall of 1000 K for all cases in the calculation.

The projectiles fly in the test section with small angles of attack. In the experiment, the pitch angle α was determined by the deviation of the base line from the vertical line in the test section. The yaw angle β was calculated from the apparent cone angle and the apparent height of the cone on the photograph. The error in the yaw angle measured by this technique is not more than 1 deg. See Ref. 16 for further details of the measurement technique.

Results

Figure 4 shows a typical example of the comparison of the calculated density contours and the experimental schlieren photograph over a sharp cone, corresponding to case 2-1. A reasonable agreement is obtained for this flowfield in terms of the shape of the shock wave.

In the present calculations, the shock layer thickness is defined by the distance between the cone surface and the shock wave, which is measured along the line normal to the cone axis in the symmetric plane. The shock wave position in the calculated flowfields is defined by the point at the maximum gradient value in the pressure distribution along the mesh line departing from the body surface. In the experiment, the photographic images were magnified and stored on a computer by using an optical scanner. The shock layer thickness was deduced from these digitized data.

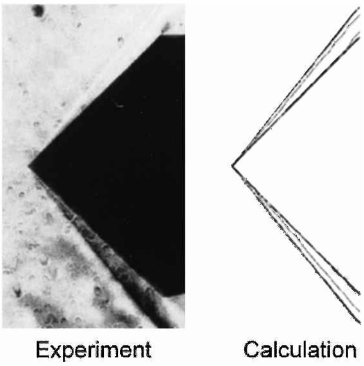

Fig. 4 Experimental photograph and calculated density for case 2-1, U_∞ = 3.31 km/s, p_∞ = 2000 Pa, pitch angle = −1.4 deg, and yaw angle = 0.0 deg.

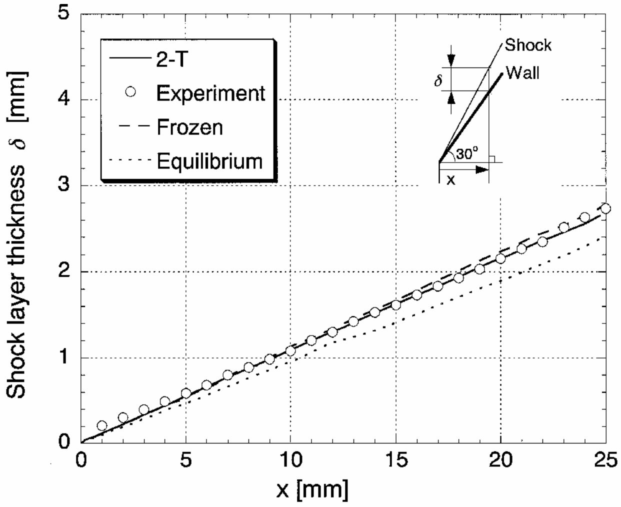

a) Windward side

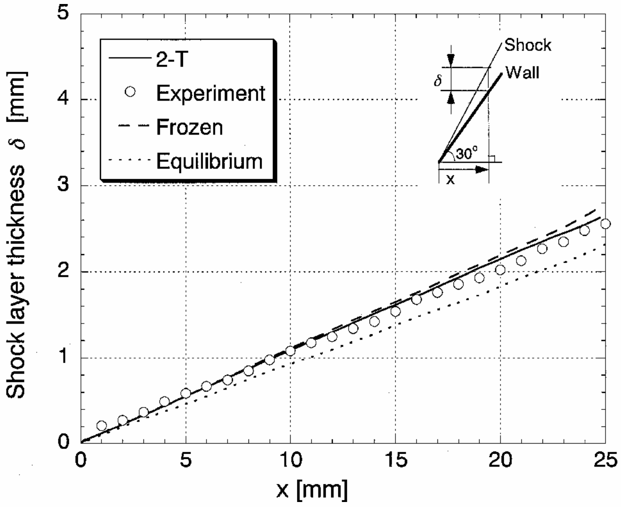

b) Leeward side

Fig. 5 Comparison of the shock layer thickness for case 1-1, U_∞ = 2.82 km/s, p_∞ = 6000 Pa, pitch angle = −0.3 deg, and yaw angle = 5.7 deg.

30-degree Sharp-Cone Flows

The calculated results of the shock layer thickness using the two-temperature model and the corresponding experimental data are compared in Figs. 5 and 6. The frozen limit and equilibrium limit of the shock shapes are also indicated. Good agreement between the two-temperature calculations and the experimental data are obtained for cases 1-1 and 1-2 on both the windward and leeward sides. The experimental data near the tip of the cone fall on the line of the frozen limit, and those in the downstream region are slightly shifted into the nonequilibrium area. These characteristics are also reproduced numerically in the two-temperature results.

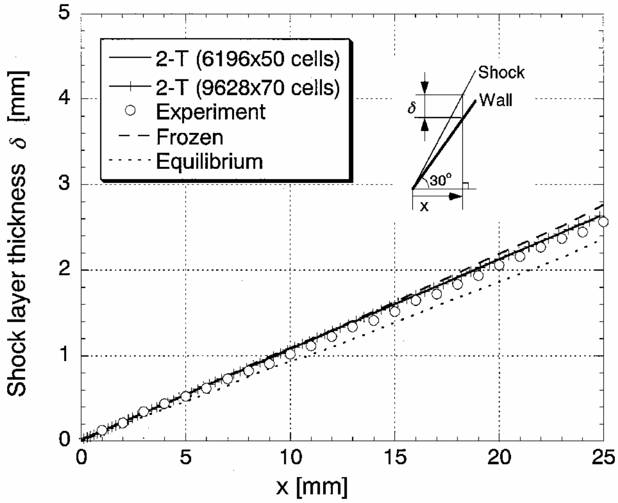

a) Windward side

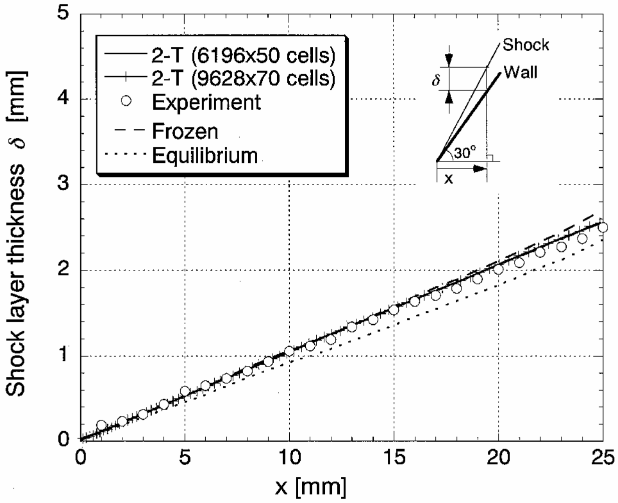

b) Leeward side

Fig. 6 Comparison of the shock layer thickness for case 1-2, U_∞ = 2.75 km/s, p_∞ = 10000 Pa, pitch angle = −1.6 deg, and yaw angle = 3.5 deg.

The percent errors of the calculated results of the shock layer thickness on the windward side are plotted in Fig. 7. We also plot the errors associated with the experimental data, which come from the model displacement during the laser irradiation and from the resolution in reading the shock position on the file.[16] One can see that errors in the calculated result for case 1-1 are very small except for the tip region. Therefore, in the downstream region, the agreement of the shock layer thickness is excellent. For case 1-2, however, the errors involved in the calculation become comparable with that of the experiment and slightly exceed them in the downstream region. Therefore, for case 1-2, the agreement is rather modest. Note that the shock layer thickness for a 30-deg sharp cone is relatively thin, and hence a small difference in the shock layer thickness can result in a larger percent error.

Figure 8 shows the temperature profiles for case 1-2 along the lines perpendicular to the axis of the cone in the symmetric plane. The translational temperature is less than 2000 K in the shock layer, and the vibrational temperature monotonically decreases from the wall to the shock wave. Chemical reactions are almost absent due to the lower temperature in the shock layer. The fraction of O atoms that are produced by dissociation reactions is less than 10^{-10} at most, although the profiles are not shown here.

For the mesh convergence study, a calculation using a finer mesh system with 9628 × 70 cells is carried out for case 1-2. The

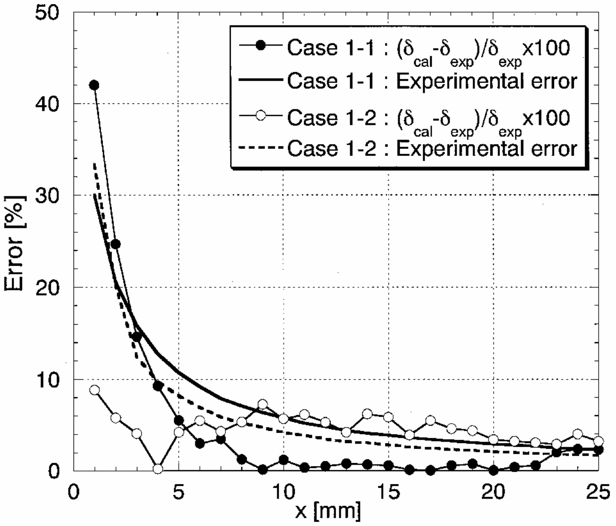

Fig. 7 Percent errors of the calculated results of the shock layer thickness compared to the experimental data for cases 1-1 and 1-2.

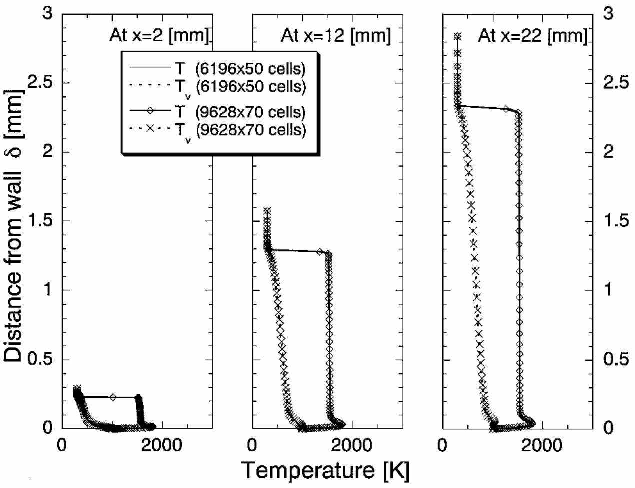

Fig. 8 Temperature profiles in the shock layer at various positions measured from the tip of the cone for case 1-2, U_∞ = 2.75 km/s, p_∞ = 10,000 Pa, pitch angle = −1.6 deg, and yaw angle = 3.5 deg.

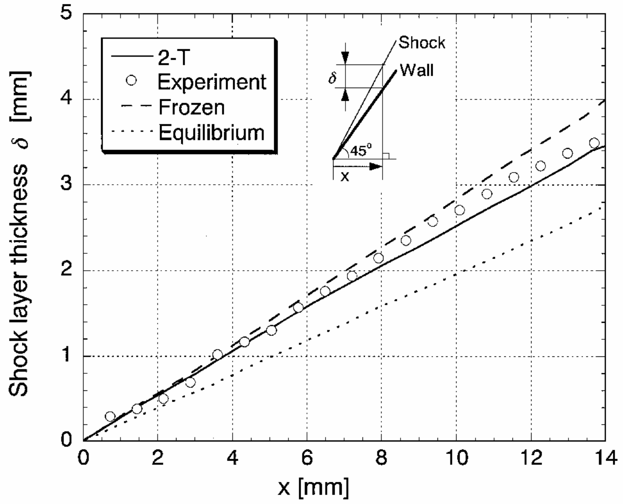

a) Windward side

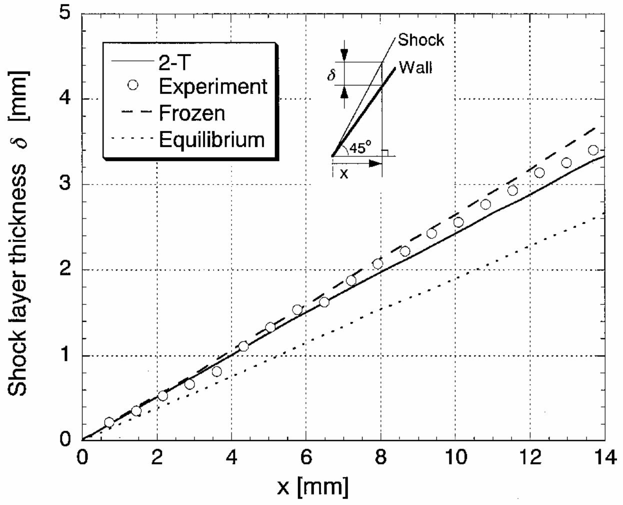

b) Leeward side

Fig. 9 Comparison of the shock layer thickness for case 2-1, U_∞ = 3.31 km/s, p_∞ = 2000 Pa, pitch angle = −1.4 deg, and yaw angle = 0.0 deg.

calculated results of the shock layer thickness and the temperature profiles are shown in Figs. 6 and 8, respectively. These profiles are identical to the calculated results using the present mesh system, which suggests that the present results give the mesh-converged solutions.

45-degree Sharp-Cone Flows

Figures 9a and 9b show the comparisons of the calculated shock layer thickness and the experimental data for case 2-1 on the windward and leeward sides, respectively. Reasonable agreement between the two-temperature calculation and the experimental data is obtained near the tip of the cone on both sides. However, the calculated shock layer thickness begins to depart from the experimental data in the downstream region. This discrepancy in the downstream region is more clearly shown in case 2-2, as can be seen in Figs. 10a and 10b. The two-temperature results fall in between the two limiting cases, which implies that the flowfields are in nonequilibrium. On the other hand, the experimental data fall in the line of the frozen limit, particularly on the leeward side.

The percent errors of the calculated shock layer thickness on the windward side for cases 2-1 and 2-2 are shown in Fig. 11. One can see the maximum error of the calculated shock layer thickness in the downstream region becomes as large as 7% in case 2-1 and 10% in case 2-2. Particularly in case 2-2, the maximum error is about twice of the experimental error. Therefore, we can say that the calculated shock layer thickness is indeed different from that obtained in the experiment.

The temperature profiles along the lines perpendicular to the axis of the cone in the symmetric plane for case 2-2 are shown in Fig. 12a. The temperature profiles at $x = 2$ mm indicate that the vibrational excitation is weak, that is, the flowfield near the tip of the cone is nearly thermally frozen. The vibrational excitations become notable approaching the downstream region. Even then, thermal equilibration is reached only at the edge of the boundary layer. The mole fraction profiles of O, N, and NO along the same lines are shown in Fig. 12b. The profiles show that the fractions of these three species gradually increase toward the downstream. However, the amount of these chemical species is insignificant throughout the shock layer, because the translational temperature in the shock layer is not high enough to initiate significant dissociation reactions.

As a part of the grid convergence study, the mesh convergence in the body-normal direction is examined for case 2-2 by employing the Richardson extrapolation procedure (see Ref. 17). Three mesh systems, namely, mesh 1, 2, and 3, are used. Mesh 2 is the original mesh system with 4612 × 50 cells. Mesh 1 is a finer mesh system with 4612 × 100 cells, and mesh 3 is a coarser one with 4612 × 25 cells. Following the method described in Ref. 18, the error of the shock layer thickness produced by Mesh k is estimated as

$$\text{percent error of } f_k = 100(f_k - f_{\mathrm{RE}})/f_{\mathrm{RE}} \qquad (12)$$

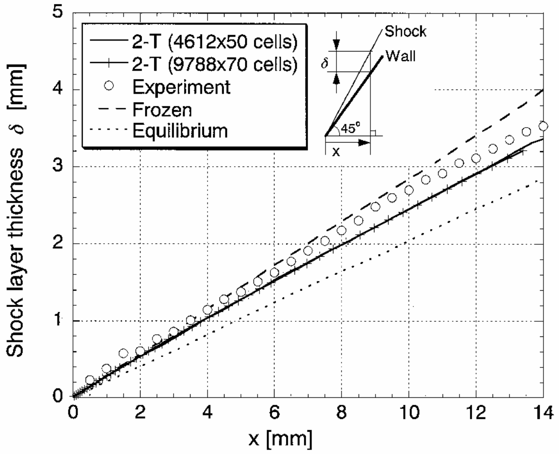

a) Windward side

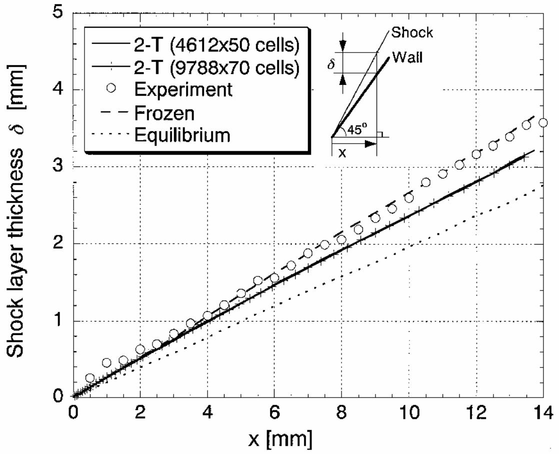

b) Leeward side

Fig. 10 Comparison of the shock layer thickness for case 2-2, U_∞ = 3.15 km/s, p_∞ = 6000 Pa, pitch angle = −1.4 deg, and yaw angle = 1.9 deg.

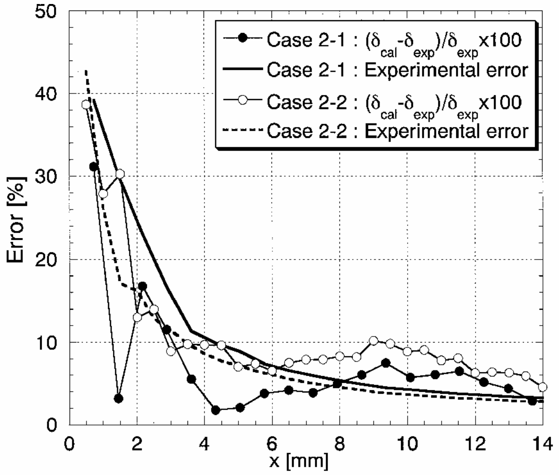

Fig. 11 Percent errors of the calculated results of the shock layer thickness compared to the experimental data for cases 2-1 and 2-2.

where f_{RE} is the extrapolated results by using the Richardson extrapolation procedure, that is, $f_{\mathrm{RE}} = f_1 + (f_1 - f_2)/3$ for a second-order numerical scheme. If mesh refinement is sufficient to be in the second-order asymptotic range, the errors on these three meshes will obey the following relationship[18]:

$$\text{percent error of } f_1 = \frac{\text{percent error of } f_2}{4} = \frac{\text{percent error of } f_3}{16} \tag{13}$$

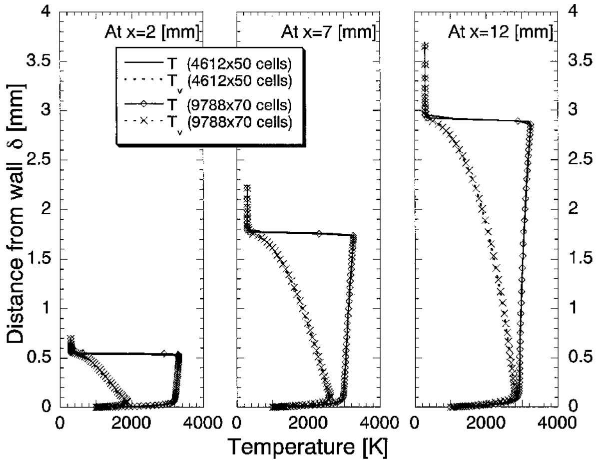

a) Temperature

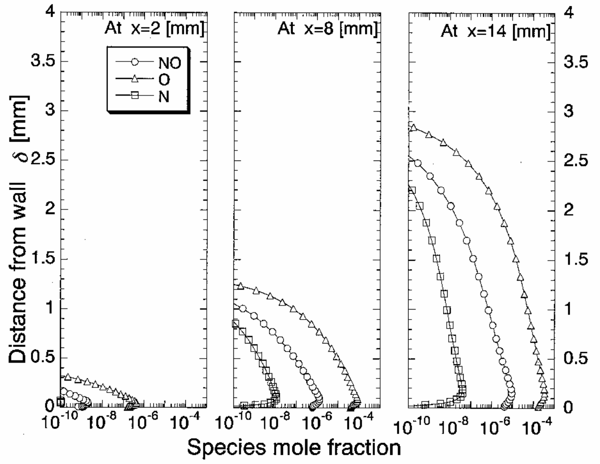

b) Species mole fraction

Fig. 12 Profiles in the shock layer at various positions measured from the tip of the cone for case 2-2, U_∞ = 3.15 km/s, p_∞ = 6000 Pa, pitch angle = −1.4 deg, yaw angle = 1.9 deg, and windward side.

Figure 13 shows the percent errors obtained on each mesh system. The shock layer thickness over the cone appears to be grid converged because the errors by each mesh system are generally very small and Eq. (13) is amply satisfied. The errors are within 0.5% all over the body surface except at the tip, where the maximum error becomes as large as 3%. Note that these errors are far smaller than the percent errors shown in Fig. 11.

A conventional mesh-convergence study for case 2-2 is also performed using a finer mesh system with 9788 × 70 cells. The shock layer thickness in Fig. 10 and the temperature profiles in Fig. 12 show excellent agreement between the calculated results using the present and the finer mesh systems. This again suggests that the present calculations with 4612 × 50 cells provide the mesh-converged solutions.

Effect of Wall Temperature on Shock Layer Thickness

The wall temperature is an important factor that determines the gas properties in the boundary layer and, hence, the displacement thickness. To investigate the influence of the wall temperature on the shock layer thickness, a parametric study is performed. The calculations assuming the wall temperature values of 293, 1000, and 2000 K are carried out for case 2-2. Figure 14 shows the comparison of obtained shock layer thickness. One can see the influence of wall temperature on the shock layer thickness is negligibly small.

Effect of Nose Tip Bluntness on Shock Layer Thickness

The projectiles used in the experiments can have finite tip bluntness. In the flow over a blunt cone, a bow shock wave can be

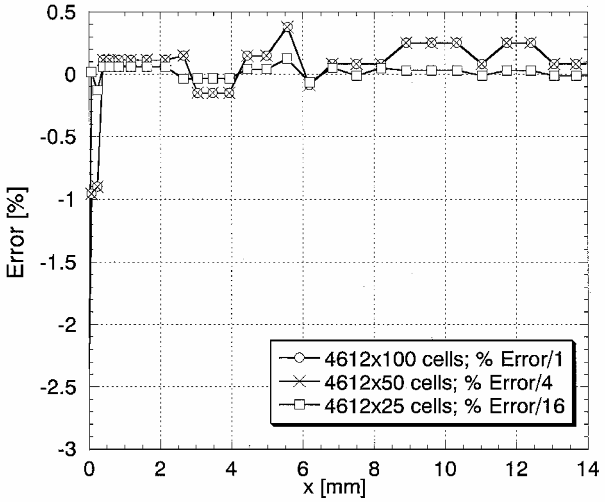

Fig. 13 Spatial error in the shock layer thickness for case 2-2.

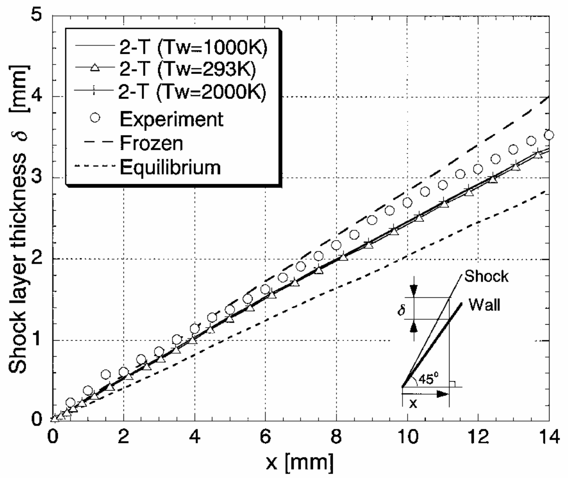

Fig. 14 Effect of wall temperature on the shock layer thickness for case 2-2.

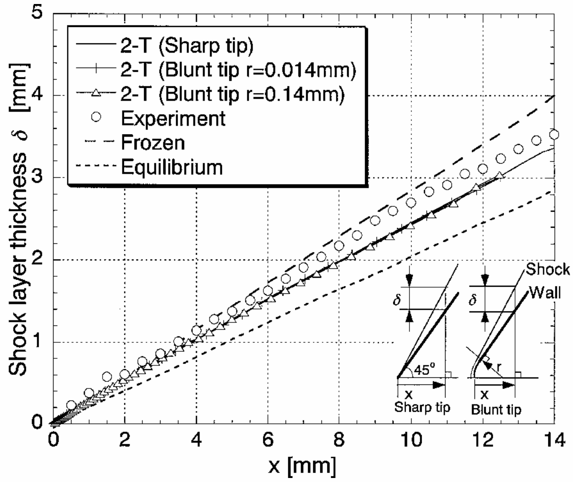

Fig. 15 Effect of tip bluntness on the shock layer thickness for case 2-2.

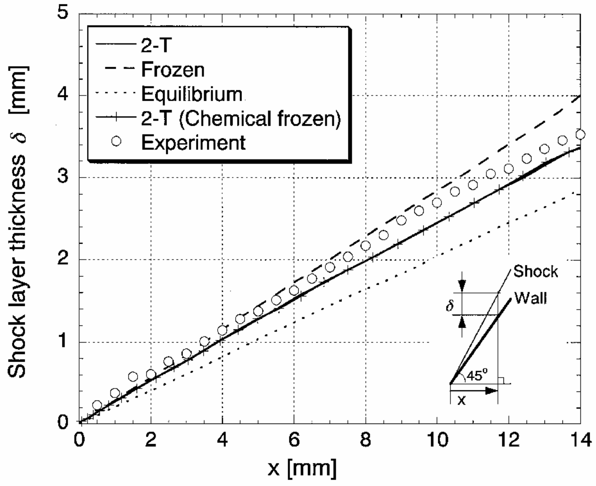

Fig. 16 Effect of chemical reactions on the shock layer thickness for case 2-2.

developed to induce a strong entropy layer that can alter the flow properties in the downstream region. To see the possible effect of tip bluntness on the shock shape, the calculations are carried out for case 2-2, assuming small tip bluntness. Tip radii of 0.014 mm and 0.14 mm are arbitrarily chosen in the calculations. The calculated results, shown in Fig. 15, indicate that the tip bluntness of the present size has little effect on the shock layer thickness.

Effect of Chemical Reactions on Shock Layer Thickness

Because dissociation reactions are endothermic, the shock layer thickness decreases because of the heat absorption if they occur. Although dissociation reactions are insignificant in the present flowfield, what, if any, chemical reactions are contributing to the reduction of the shock layer thickness observed in case 2-2 is explored by forbidding the dissociation reactions. The comparison of the shock layer thickness shown in Fig. 16 clearly indicates that chemical reactions have no consequence on the shock layer thickness for the present case.

Effect of Assigning Single Vibrational Temperature

In the two-temperature model, the same vibrational temperature is assigned to both O_2 and N_2 molecules. However, the behavior of the vibrational excitation of O_2 and N_2 can be quite different and could have some effect on the shock layer thickness. A three-temperature model that defines one translational temperature and two vibrational temperatures corresponding to O_2 and N_2 is employed in the calculation of the flowfield for case 2-2. We assume that the vibrational temperature of NO is in equilibrium with that of O_2 because NO is a minor molecular species in the present case. Two different vibrational–electronic energy conservation equations corresponding to O_2 and NO and N_2 are solved in the calculation. The rate-controlling temperature of the dissociation reaction of species s is defined by $T_a = \sqrt{(T T_{vs})}$ instead of Eq. (3). The vibrational source term for species s is given by $W_{vs} = W_{v-Ts} + W_{C-vs}$ instead of Eq. (8). The remaining descriptions of the two-temperature model related to chemical reactions and vibrational excitations are retained. The vibrational–vibrational coupling between O_2 and N_2 molecules is simply ignored for obtaining a larger shock layer thickness. As shown in Fig. 17, the shock layer thickness calculated by the present three-temperature model is slightly larger than that given by the two-temperature calculation. However, the overall agreement with experimental data is not improved at all.

Sensitivity to Freestream Conditions

The characterized freestream conditions in the experiment inevitably involve some uncertainties. We have examined the sensitivity of the shock layer thickness to the variation of the freestream conditions. The uncertainties in the freestream conditions are evaluated as follows.[16] The uncertainty in the flight velocity of the projectile is ±0.8% in the test section. The static pressure in the test section has an uncertainty of ±10 Pa, which comes from a reading error of the manometer when the test section is vacuumed. The freestream temperature in the test section varies in the range of 293 ± 3 K. The estimated uncertainties involved in the pitch and yaw angles of the projectile are less than 1 deg.

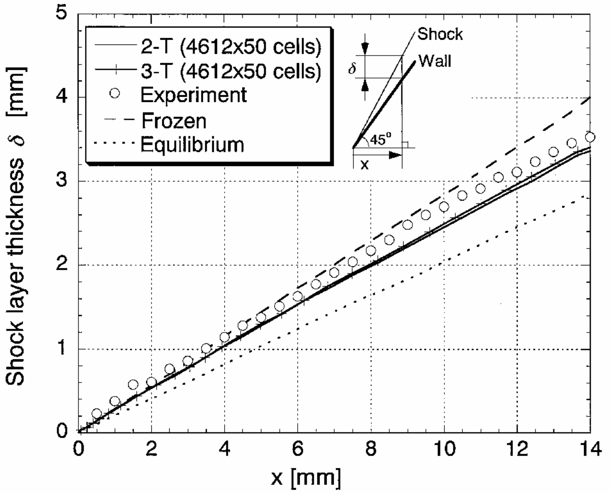

Fig. 17 Comparison of the shock layer thickness for case 2-2 calculated by two-temperature and three-temperature models.

A series of test calculations in which the boundary conditions are varied to account for these uncertainties are carried out for case 2-2. The obtained results do not show any significant change in the shock layer thickness. Therefore, we can say that the calculated shock layer thickness is insensitive to the possible uncertainties involved in the freestream conditions.

Discussion

The calculated shock shapes over sharp cones are compared with the experimental data for the different static pressure values at the flight velocity of about 3.0 km/s. The two-temperature calculations well reproduce the corresponding experimental data for the 30-deg sharp cone in both cases 1-1 and 1-2, in which vibrational excitations and chemical reactions are found to be absent. However, considerable distinctions between the two-temperature calculations and the experimental data are noticed in the results for the 45-deg sharp cone in cases 2-1 and 2-2, when vibrational excitation begins to occur in the downstream region. A similar observation was made in our previous study, in which the calculated shock standoff distance for a sphere flying at the same velocity range was found to be shorter than that given by the ballistic range experiment. The flowfield developed over a sphere was chemically nearly frozen and vibrationally excited. (See case 1-3 in Ref. 5.)

To identify the possible cause, we have carried out several numerical experiments for case 2-2 where the discrepancy with the experimental data was most significant. What we have examined are 1) influence of wall temperature, 2) influence of tip bluntness, and 3) influence of assigning a single vibrational temperature. However, none of these influences could change the shock shape considerably and, therefore, improve the agreement between the calculated shock shape and that given by the corresponding experimental data. Nor was the agreement improved when dissociation reactions in the shock layer were forced to be absent.

As already noted, the calculated flowfield developed over a sphere in our previous study was found to be nearly frozen and vibrationally excited. We found that agreement of the calculated shock standoff distance with that given in the ballistic range experiment was not improved even if dissociation reactions were prohibited. This is also found to be the case in the present study. The calculated results indicate that the present flowfield is almost chemically frozen. Therefore, the chemical reactions are not likely the cause of the thinner shock layer.

What the true origin is of the observed discrepancy in the shock layer thickness is yet an open question. In Ref. 19, we found that the shock standoff distance over a sphere could be larger if rotational nonequilibrium was introduced and a larger collision number was assumed. However, the agreement with the corresponding experimental data was obtained only when a substantially longer translational–vibrational relaxation time was additionally assumed. It is our common experience that the calculated shock layer thickness tends to be thinner than the experimental data when vibrational excitation occurs in otherwise chemically and vibrationally frozen flowfield. The evidence suggests that the translational–vibrational relaxation process has a close connection with the appearance of the thinner shock layer. Indeed, one can make the calculated shock layer thickness agree with the experimental data if a sufficiently long vibrational relaxation time is employed. However, such an argument apparently contradicts the well-known Millikan–White (M–W) correlation[20] for vibrational relaxation time that is commonly employed in hypersonic CFD calculations and thus leads to a dead end.

There seems to exist one possible scenario that does not violate the M–W correlation and yet can give a thicker shock layer. Remember that the M-W correlation is derived with an assumption that translational and rotational energy modes are always in equilibrium. When a significant rotational nonequilibrium comes out behind the shock wave, the apparent vibrational relaxation rate becomes smaller than that given by the M–W correlation due to the lower rotational temperature. This smaller vibrational relaxation rate can make the shock layer thicker. In Ref. 19, we ignored this effect and employed the M–W correlation in original form for assigning the vibrational relaxation rate. For this scenario to take place, a collision number that is substantially larger than that given by the standard Parker model[21] is needed. There is some experimental evidence that implies larger collision numbers are needed for rotational relaxation behind strong shock waves.[22,23] It is not clear, however, whether such significant rotational nonequilibrium can be developed behind the shock wave in the intermediate hypersonic regime. Further studies are obviously needed to see the consequence.

Conclusions

Shock shapes over sharp cones flying at a velocity of 3.0 km/s are calculated by the thermochemical nonequilibrium CFD code using the existing two-temperature model. The obtained results for 30-deg sharp cone show good agreement with the experimental data obtained in a ballistic range. However, the calculated shock layer thickness of the 45-deg sharp cone tends to be thinner than the experimental data. The discrepancy becomes apparent in the downstream region, where flowfield is in chemically frozen but vibrationally excited. Various effects that might have an impact on the shock layer thickness are examined, but none of them could improve the agreement. It is implied that vibrational excitation has a close connection with the thinner shock layer. This tendency is consistent with what we have found in our previous study of the shock standoff distance for a sphere in intermediate hypersonic flow.

Acknowledgments

This work has been supported by the Research Fellowships of the Japan Society for the Promotion of Science for Young Scientists.

References

[1] Nonaka, S., and Takayama, K., "Measurement of Shock Standoff Distance for Sphere in Ballistic Range," *Journal of Thermophysics and Heat Transfer*, Vol. 14, No. 2, 2000, pp. 225–229.

[2] Nonaka, S., and Takayama, K., "Ballistic Range Measurement of the Shock Shapes in Intermediate Hypersonic Regime," AIAA Paper 99-1025, Jan. 1999.

[3] Park, C., "Validation of CFD Codes for Real-Gas Regime," AIAA Paper 97-2530, June 1997.

[4] Park, C., "Assessment of Two-Temperature Kinetic Model for Ionizing Air," *Journal of Thermophysics and Heat Transfer*, Vol. 3, No. 3, 1989, pp. 233–244.

[5] Furudate, M., Nonaka, S., and Sawada, K., "Behavior of Two-Temperature Model in Intermediate Hypersonic Regime," *Journal of Thermophysics and Heat Transfer*, Vol. 13, No. 4, 1999, pp. 424–430.

[6] Anderson, J. D., Jr., *Hypersonic and High Temperature Gas Dynamics*, McGraw–Hill, 1989, pp. 548–590.

[7] Park, C., *Nonequilibrium Hypersonic Aerothermo-dynamics*, Wiley, New York, 1989.

[8] Sharma, S. P., Hou, W., and Park, C., "Rate Parameters for Coupled Vibration–Dissociation in a Generalized SSH Approximation," *Journal of Thermophysics and Heat Transfer*, Vol. 6, No. 1, 1992, pp. 9–21.

[9] Blottner, F. G., Johnson, M., and Ellis, M., "Chemically Reacting Viscous Flow Program for Multi-Component Gas Mixture," Sandia National Labs. Rept. SC-RR-70-754, Albuquerque, NM, Dec. 1971.

[10] Vincenti, W. G., and Kruger, C. H., *Introduction to Physical Gas Dynamics*, Wiley, New York, 1967, pp. 375–435.

[11] Wilke, C. R., "A Viscosity Equation for Gas Mixtures," *Journal of Chemical Physics*, Vol. 18, No. 4, 1950, pp. 517–519.

[12] Wada, Y., and Liu, M. S., "A Flux Splitting Scheme with High-Resolution and Robustness for Discontinuities," AIAA Paper 94-0083, Jan. 1994.

[13] Anderson, W. K., Thomas, J. L., and van Leer, B., "Computation of Finite Volume Flux Vector Splitting for the Euler Equations," *AIAA Journal*, Vol. 24, No. 9, 1986, pp. 1453–1460.

[14] Barth, T. J., "Aspect of Unstructured Grid and Finite-Volume Solvers for the Euler and Navier–Stokes Equations," AGARD-R-787, May 1992, pp. 6/1–6/61.

[15] Eberhardt, S., and Imlay, S., "Diagonal Implicit Scheme for Computing Flows with Finite Rate Chemistry," *Journal of Thermophysics and Heat Transfer*, Vol. 6, No. 2, 1992, pp. 208–216.

[16] Nonaka, S., "Experimental and Numerical Study on Hypersonic Flows in Ballistic Range," Ph.D. Dissertation, Dept. of Aeronautics and Space Engineering, Tohoku Univ., Sendai, Japan, Jan. 2000.

[17] Roache, P. J., "Perspective: A Method for Uniform Reporting of Grid Refinement Studies," *Journal of Fluids Engineering*, Vol. 116, No. 3, 1994, pp. 405–413.

[18] Roy, C. J., and Bartel, T. J., "DSMC and Navier–Stokes Predictions for Hypersonic Laminar Interacting Flows," AIAA Paper 2001-1030, Jan. 2001.

[19] Furudate, M., and Sawada, K., "Effect of Rotational Nonequilibrium on Shock Standoff Distances in Intermediate Hypersonic Range," AIAA Paper 2001-0813, Jan. 2001.

[20] Millikan, R. C., and White, D. R., "Systematic of Vibrational Relaxation," *Journal of Chemical Physics,* Vol. 39, No. 12, 1963, pp. 3209–3213.

[21] Parker, J. G., "Rotational and Vibrational Relaxation in Diatomic Gases," *Journal of Fluids*, Vol. 2, No. 4, 1991, pp. 449–462.

[22] Sharma, S. P., and Gillespie, W., "Nonequilibrium and Equilibrium Shock Front Radiation Measurements," *Journal of Thermophysics and Heat Transfer*, Vol. 5, No. 3, 1991, pp. 257–265.

[23] Fujita, K., Sato, S., Abe, T., and Ebinuma, Y., "Experimental Investigation of Air Radiation Behind a Strong Shock Wave," *Journal of Thermophysics and Heat Transfer*, Vol. 16, No. 1, 2002, pp. 77–82.